

## RESEARCH OUTPUTS / RÉSULTATS DE RECHERCHE

### Metallic Nanoparticles

Penninckx, Sebastien; Hespeels, Felicien; Smeets, Julien; Colaux, Julien; Lucas, Stephane; Heuskin, Anne-Catherine

*Published in:*  
Radiation

*DOI:*  
[10.3390/radiation1040025](https://doi.org/10.3390/radiation1040025)

*Publication date:*  
2021

#### [Link to publication](#)

*Citation for published version (HARVARD):*

Penninckx, S, Hespeels, F, Smeets, J, Colaux, J, Lucas, S & Heuskin, A-C 2021, 'Metallic Nanoparticles: A Useful Prompt Gamma Emitter for Range Monitoring in Proton Therapy?', *Radiation*, vol. 1, no. 4, pp. 305-316. <https://doi.org/10.3390/radiation1040025>

#### General rights

Copyright and moral rights for the publications made accessible in the public portal are retained by the authors and/or other copyright owners and it is a condition of accessing publications that users recognise and abide by the legal requirements associated with these rights.

- Users may download and print one copy of any publication from the public portal for the purpose of private study or research.
- You may not further distribute the material or use it for any profit-making activity or commercial gain
- You may freely distribute the URL identifying the publication in the public portal ?

#### Take down policy

If you believe that this document breaches copyright please contact us providing details, and we will remove access to the work immediately and investigate your claim.

## Article

# Metallic Nanoparticles: A Useful Prompt Gamma Emitter for Range Monitoring in Proton Therapy?

Sébastien Penninckx <sup>1,2,†</sup>, Félicien Hespeels <sup>1,3,†</sup>, Julien Smeets <sup>4</sup>, Julien L. Colaux <sup>5</sup>, Stéphane Lucas <sup>1</sup> and Anne-Catherine Heuskin <sup>1,\*</sup>

- <sup>1</sup> Laboratory of Analysis by Nuclear Reactions, NAMur Research Institute for Life Sciences, University of Namur, Rue de Bruxelles, 61, 5000 Namur, Belgium; sebastien.penninckx@unamur.be (S.P.); felicien.hespeels@uclouvain.be (F.H.); stephane.lucas@unamur.be (S.L.)
- <sup>2</sup> Medical Physics Department, Jules Bordet Institute, Université Libre de Bruxelles, 1 Rue Héger-Bordet, 1000 Brussels, Belgium
- <sup>3</sup> Medical Physics Department, Clinique & Maternité Sainte-Elisabeth, Place Louise Godin 15, 5000 Namur, Belgium
- <sup>4</sup> Ion Beam Applications S.A., Chemin du Cyclotron 3, 1348 Louvain-la-Neuve, Belgium; Julien.Smeets@iba-group.com
- <sup>5</sup> Namur Institute of Structured Matter (NISM), Synthesis, Irradiation and Analysis of Materials Platform (SIAM), University of Namur, Rue de Bruxelles, 61, 5000 Namur, Belgium; julien.colaux@unamur.be
- \* Correspondence: anne-catherine.heuskin@unamur.be
- † Authors contributed equally.

**Simple Summary:** This study provides the proof-of-concept of metal-based nanoparticles, injected into tumor, as a prompt gamma (PG) enhancer, assisting beam range verification, which presents a major challenge in protontherapy treatment. We showed that metallic nanoparticles can increase the yield of PG after interaction with an incident proton beam via specific nuclear reactions. We investigated the applicability of this technology in different clinical scenarios and identified that the PG camera design and nanoparticles biodistribution in the patient body are the two main limiting factors to allow for a successful clinical translation.

**Abstract:** In clinical practice, dose delivery in proton therapy treatment is affected by uncertainties related to the range of the beam in the patient, which requires medical physicists to introduce safety margins on the penetration depth of the beam. Although this ensures an irradiation of the entire clinical target volume with the prescribed dose, these safety margins also lead to the exposure of nearby healthy tissues and a subsequent risk of side effects. Therefore, non-invasive techniques that allow for margin reduction through online monitoring of prompt gammas emitted along the proton tracks in the patient are currently under development. This study provides the proof-of-concept of metal-based nanoparticles, injected into the tumor, as a prompt gamma enhancer, helping in the beam range verification. It identifies the limitations of this application, suggesting a low feasibility in a realistic clinical scenario but opens some avenues for improvement.

**Keywords:** prompt gamma; nanoparticles; proton therapy; radioenhancer; radiosensitizer



**Citation:** Penninckx, S.; Hespeels, F.; Smeets, J.; Colaux, J.L.; Lucas, S.; Heuskin, A.-C. Metallic Nanoparticles: A Useful Prompt Gamma Emitter for Range Monitoring in Proton Therapy? *Radiation* **2021**, *1*, 305–316. <https://doi.org/10.3390/radiation1040025>

Academic Editor: Gabriele Multhoff

Received: 2 October 2021

Accepted: 25 November 2021

Published: 30 November 2021

**Publisher's Note:** MDPI stays neutral with regard to jurisdictional claims in published maps and institutional affiliations.



**Copyright:** © 2021 by the authors. Licensee MDPI, Basel, Switzerland. This article is an open access article distributed under the terms and conditions of the Creative Commons Attribution (CC BY) license (<https://creativecommons.org/licenses/by/4.0/>).

## 1. Introduction

Therapies based on charged particles such as proton and carbon-ion therapy are attracting interest due to the favorable ballistic properties of ion-matter interaction. The characteristic Bragg peak allows for the shaping of the deposited dose distribution, thereby maximizing tumor targeting while sparing the surrounded healthy tissue [1]. This presents a clear advantage over classical X-ray radiotherapy, especially for a tumor located in front of organs that are at risk, since the dose-depth profile reduces rapidly to zero after the Bragg peak resulting in a dose deposition in deeper tissues. However, this ballistic benefit also makes hadrontherapy more prone to errors. Since the stopping power of a proton

depends on the exact composition of tissues encountered by the beam, hadrontherapy is quite sensitive to any potential source of deviation such as organ motion, patient mispositioning or anatomic changes between dose fractions [2]. Moreover, uncertainties arise from the treatment planning since the patient-specific proton stopping power values are deduced from computed tomography images via a conversion of the X-ray attenuation coefficient to the stopping power [3,4]. By taking into account imaging modalities, patient setup, beam delivery and dose calculation, Paganetti et al. estimated a total proton range uncertainty of 2.7% + 1.2 mm [5]. In clinical practice, this leads to the introduction of safety margins in the treatment planning in order to ensure an irradiation of the entire clinical target volume with the prescribed dose. However, these safety margins lead to nearby healthy tissues becoming exposed, and a subsequent risk of side effects. Therefore, the interest for a non-invasive technique that allows for margin reduction through the on-line monitoring of the beam range is growing [6].

Different approaches are currently under development to monitor the ion range in patients. Most of them are based on the analysis of secondary products issued from ion–matter interaction during irradiation, including neutrons [7,8], ultrasounds [9,10], positrons [11,12], electron-bremsstrahlung [13] or gamma photons. Among them, the detection of prompt-gamma (PG) radiations for beam range monitoring has several advantages. Due to their high energy (mostly from 1 to 8 MeV), gamma photons have a high probability to exit the patient body without any interaction on their way out, ensuring undisturbed information. As the PG emission immediately follows the interaction between the incident particle and the tissue nuclei, its use can manage the time structure and intensities of treatment beams in the therapy facility. Finally, a strong correlation is expected between the PG spectra and the proton range, so as to accurately pinpoint the Bragg peak position [14,15].

Since Stichelbaut and Jongen first proposed the use of PG detection to monitor beam range in 2003 [16], this idea has been tested in clinical setups [17,18]. This development was achieved as a result of Monte Carlo (MC) simulation codes that have the potential to fully describe the nuclear processes that lead to secondary radiation emission [19–21]. Initial studies focusing on PG emission reproduction were performed with Geant4 [22,23].

The development of nanomedicine has become one of the leading areas in the fight against cancer, with first-generation candidates reaching clinical trials. The ability of metal-based nanoparticles to amplify proton radiation treatment efficiency was demonstrated, highlighting their potential use to decrease dose delivered to the patient and any subsequent healthy tissue side effects [24–26]. Indeed, the presence of these nano-objects in the planning tumor volume (PTV) increases the mean tissue density, resulting in a higher proton stopping power when the charged particle crosses the target volume. Although this hypothesis was largely studied in terms of the radiosensitization mechanism, the opportunity to use them as a PG signal enhancer remains poorly investigated. By increasing the energy deposited in the PTV, the number of detected PG can be maximized so as to gather valuable information on beam range. In the framework of this study, we investigated the coupling of the well-described radiosensitizer role of metallic nanoparticles with a potential PG yield-enhancer effect.

## 2. Materials and Methods

### 2.1. Geant4 Monte Carlo Simulations

#### 2.1.1. Physics Lists

To reproduce the stochastic nature of interactions between charged particles and the considered target (water, water with 1% mass fraction nanoparticles, bone, muscle), the resulting PG emission and its transport in solids and detection, we used simulation tools based on a Monte Carlo approach. In this study, the Geant4 10.05.p01 version was used.

The Geant4 PhysicsList used for each simulation contains builders for hadronic interactions. For electromagnetic processes, this list includes the G4EmStandardPhysics\_option3 physics. For hadronic physics, the QGSP\_BIC\_HP list is used as it was found to provide good results for proton therapy studies [27,28]. QGSP stands for the “*quark gluon string*”

*precompound*” model, BIC for “Binary Cascade”, and HP indicates that a high precision neutron tracking model is used for thermal energies up to 20 MeV.

The G4RadioactiveDecayPhysics and G4HadronElasticPhysicsHP modules were active. The point source issued 150 MeV protons in the z direction. For proton step size, a limit of 1 mm was selected to decrease the simulation duration.

### 2.1.2. Geant4 Simulation Geometry

The geometry, depicted on Figure 1, consists of a water box of a 20 cm length and 20 cm side. At a 5 cm depth, the water volume is filled with three boxes of a 2 cm length and 15 cm side, made of adipose tissue, muscle and dense bone (densities are referred in Table 1). Following the production of these layers, a 1 cm water gap and a box called “Tumor volume” of 3 cm length and 15 cm side are added. The tumor volume is either filled with water (best case scenario for optimum gamma ray yield compared to all other tissues) or with water containing 1% weight of metal (Ag, Al, Au, Bi, Cd, Gd, Hf, Si, Ti) in the case of a tumor loaded with metal-based nanoparticles. Nanoparticles are not explicitly modeled, as a 1% weight of small metal spheres would constitute a tremendous number of objects. For this reason, a mixture approach was selected. This geometry represents liver irradiation, for which some protons could pass successively through adipose tissue, intercostal muscle and one of the last ribs of the thoracic cage. Nevertheless, the dimensions do not correspond to a given clinical condition, as they vary depending on the patient.

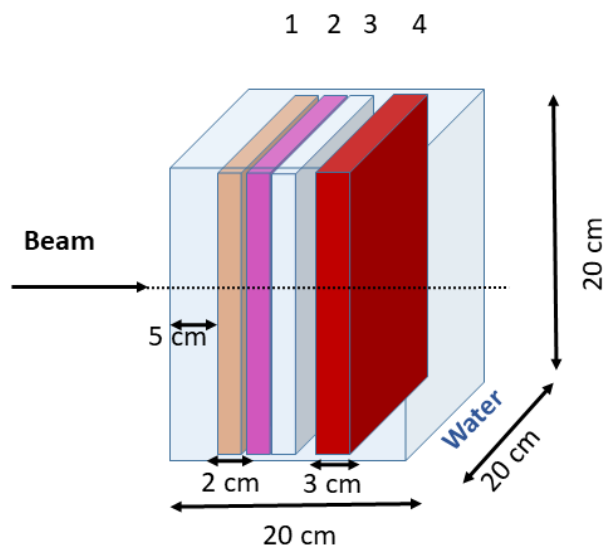


**Figure 1.** Heterogeneous target implemented in Geant4. The complete material list is: (1) adipose tissue, (2) muscle, (3) dense bone and (4) “Tumor volume”. The tumor volume material is filled with water or a mix of water with Ag, Al, Au, Bi, Cd, Gd, Hf, Si or Ti for which a mass weight of 1% is used.

**Table 1.** Material density used in Geant4.

Material	Density (g/cm <sup>3</sup> )
Adipose tissue	0.967
Water	1.000
Muscle	1.061
Dense bone	1.575

Each primary or secondary gamma is scored at creation vertex and, where appropriate, its position is reported in the beam direction (depth in tissue). The cut value has been set to 1 nm for all particle types.

Densities from the International Commission on Radiation Units and measurements (ICRU) report 37 are used for each material [29]. The density of each material is given in the table below:

### 3. Results

#### Prompt Gamma Enhancement with Nanoparticles

The tumor volume material (see Figure 1) can be filled with water or a mixture of water with nanoparticles (Ag, Al, Au, Bi, Cd, Gd, Hf, Si or Ti). The nanoparticles (NPs) number is determined based on a 1% NP mass weight condition. This concentration is comparable to the gold concentration measured by Hainfeld et al. for in vivo tumors [30–32]. The proton beam energy is set to 150 MeV. Figure 2 presents the energy deposited by the proton along its path.

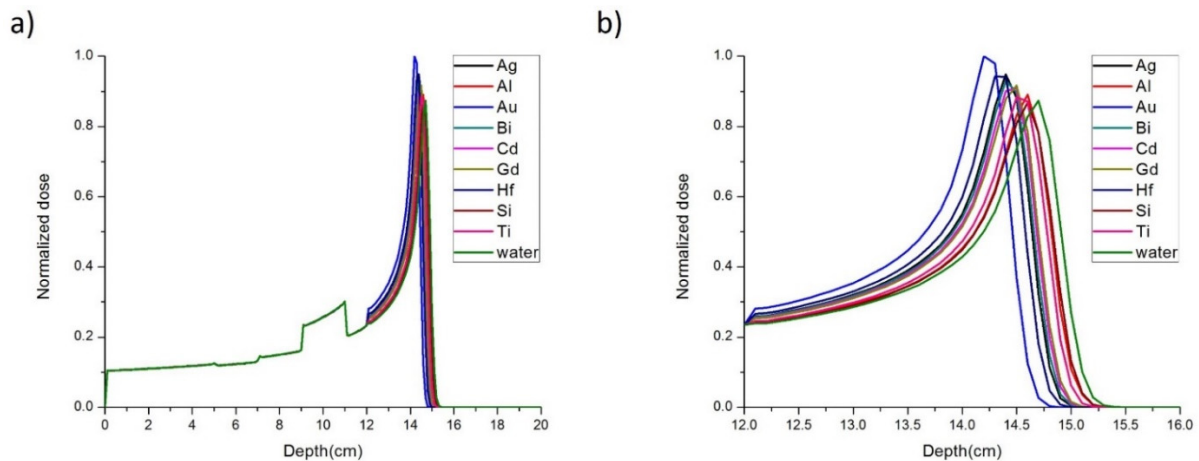


**Figure 2.** (a) Normalized dose distribution after 150 MeV proton irradiation. (b) Zoom on the “Tumor volume”.

As the “dense bone” density ( $1.575 \text{ g/cm}^3$ ) is higher than water ( $1.000 \text{ g/cm}^3$ ), a higher energy deposition is observed between a 9 and 11 cm depth. As expected, depending on the “tumor volume” composition, the energy deposited is affected and, consequently, the proton range. The lowest range is obtained in the case of an Au of 1% weight whereas the maximum range corresponds to the case of a water target (see Table 2). Figure 3 shows the PG rays longitudinal distributions after 150 MeV proton irradiation.

**Table 2.** Proton beam range at 80% BP and corresponding PG range ( $\geq 1 \text{ MeV}$ ) after 150 MeV proton irradiation.

Element	Longitudinal Beam Range (mm $\pm$ 0.1 mm)	Longitudinal PG Range (mm $\pm$ 0.1 mm)	Delta (mm $\pm$ 0.1mm)
Ag	145.5	143.4	2.1
Al	147.3	145.1	2.2
Au	143.7	141.8	1.9
Bi	145.7	143.5	2.2
Cd	146.0	143.8	2.2
Gd	146.2	144.0	2.2
Hf	145.0	142.9	2.1
Si	147.5	145.2	2.3
Ti	146.9	144.7	2.2
Water	148.3	145.9	2.4

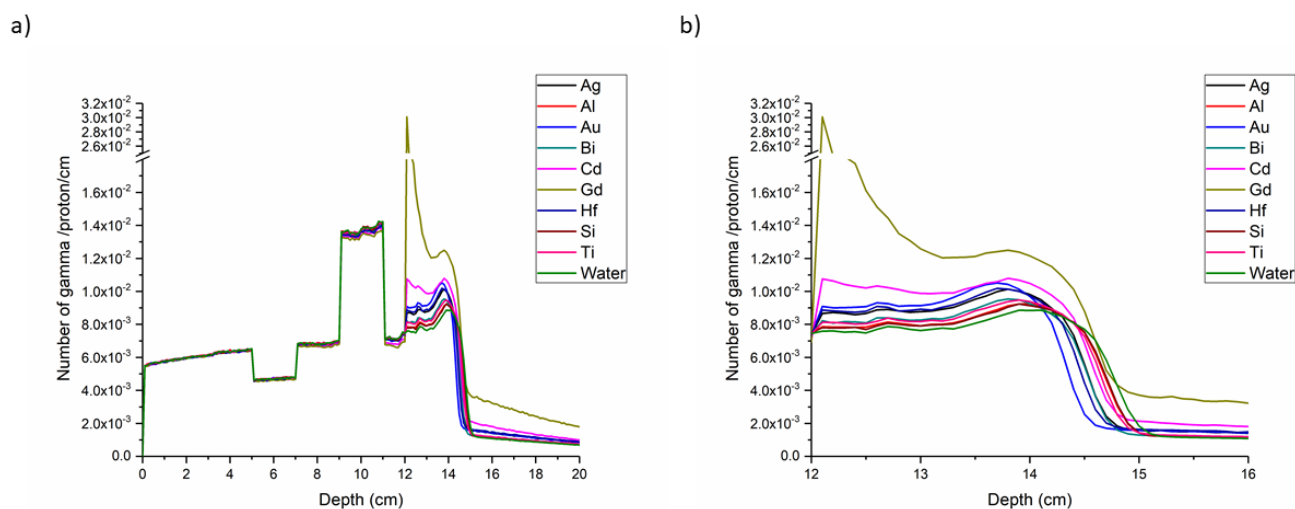


**Figure 3.** (a) Longitudinal distribution of all gamma rays (emitted with energies higher than 1 MeV) after 150 MeV proton irradiation. (b) Zoom on the “Tumor volume” (depth range: 12–16 cm).

The amount of PG emitted from Gd loaded tumor is the most significant. However, the majority of this signal is constituted by secondary PG resulting from  $(n,\gamma)$  reactions. Indeed, two gadolinium isotopes have a large capture cross section for thermal neutrons: 60,900 b for  $^{155}\text{Gd}$  (isotopic abundance 14.80%) and 254,000 b for  $^{175}\text{Gd}$  (isotopic abundance 15.65%) [33]. Since the proton range information is linked to the primary gamma rays and not the secondary gamma, the amount of secondary gamma is not relevant for range estimation.

As is similar to the energy deposition profile, a decrease in the PG yield is observed in the adipose tissue region between a 5 and 7 cm depth and an important increase can be noted between a 9 and 11 cm depth in the dense bone area. This is partly due to the stopping power value differences between both materials and additional  $(p,\gamma)$  reactions that are produced in the bone area, e.g.,  $^{31}\text{P}(p,p'\gamma)^{31}\text{P}$ , producing 1266 keV gamma or  $^{40}\text{Ca}(p,p'\gamma)^{40}\text{Ca}$  with deexcitation at 3736 keV [34,35]. In addition, the PG ray profile is dependent on the composition of the “tumor volume”.

In order to evaluate the correlation between the PG signal intensity and the BP shifts, we calculated the particle beam range and the PG range for each material. The particle range corresponds to the position of the 80% BP distal fall off. Similarly, the PG range is the position corresponding to the 80% PG emission yield fall-off. The obtained results are presented in Table 2. A significant Pearson’s correlation coefficient of 0.9993 ( $p$  value < 0.01) was calculated between the two ranges. A normalized dose and associated total PG emission are presented for water and tumor loaded with SiNP in supplemental Figure S1.

For each material, PG rays provide a high accuracy in order to estimate the proton beam range. The small 2 mm mismatch between the PG range and actual beam range is a known offset and results from the low proton energy at this depth, which is too low to drive nuclear reactions. Notably, the BP position slightly shifts to lower values when the metal atomic number increases, as expected from Bethe-Bloch formula.

In order to determine the optimal nanoparticle composition to enhance PG emission, for each nanoparticle material, the ratio between the primary gamma yield at 80% PG fall off and the secondary gamma yield at 80% PG is calculated and compared to that obtained for water alone. The results are presented in Table 3.

Among the tested metals, the maximum absolute yield for primary PG rays emission was obtained for AgNP. However, the presence of Ag, Au, Cd, Gd, Hf, and Ti nanoparticles lead to a decrease in the primary to secondary PG ratio when compared to water. The proton range information is linked to the primary gamma rays and the secondary gamma rays could lead to significant interference on the BP tracking. Therefore, the best choice corresponds to the one that maximizes the primary PG emission yield compared to the

secondary PG emission yield. From Table 3, it can be observed that AlNP, BiNP and SiNP are the best suited. The ratio between primary and secondary PG yield is increased by 6%, 3% and 3% for SiNP, AlNP and BiNP, respectively, compared to water. Among these, the maximum absolute yield for primary PG ray emission is obtained for BiNP. The presence of Ag, Au, Cd, Gd, Hf, and Ti nanoparticles leads to a decrease in the primary to secondary PG ratio when comparing to water. If we assume a 2 Gy dose deposition (typical value of dose per fraction in daily radiotherapy sessions) delivered as pristine peaks, this corresponds to  $1.68 \times 10^{11}$  protons passing through the tumor volume in our configuration. This means that the presence of 1% Si NP in the tumor volume leads to  $8 \times 10^6$  additional primary PG compared to the water control.

**Table 3.** Comparison between primary gamma and secondary gamma enhancement at 80% PG fall off.

Element	Number of Primary PG per Incident Proton	Number of Secondary PG per Incident Proton	Ratio (Primary/Secondary PG)	Fold Change with Respect to Water
Ag	$6.72 \times 10^{-4}$	$1.73 \times 10^{-4}$	3.88	0.86
Al	$6.17 \times 10^{-4}$	$1.32 \times 10^{-4}$	4.66	1.03
Au	$6.33 \times 10^{-4}$	$1.76 \times 10^{-4}$	3.60	0.80
Bi	$6.66 \times 10^{-4}$	$1.43 \times 10^{-4}$	4.66	1.03
Cd	$6.03 \times 10^{-4}$	$2.35 \times 10^{-4}$	2.56	0.57
Gd	$6.07 \times 10^{-4}$	$4.05 \times 10^{-4}$	1.50	0.33
Hf	$6.20 \times 10^{-4}$	$1.80 \times 10^{-4}$	3.45	0.76
Si	$6.24 \times 10^{-4}$	$1.30 \times 10^{-4}$	4.79	1.06
Ti	$5.84 \times 10^{-4}$	$1.42 \times 10^{-4}$	4.10	0.91
Water	$5.75 \times 10^{-4}$	$1.28 \times 10^{-4}$	4.51	1.00

Some particular spectroscopic features were found in the energy spectra. Figure 4 shows the total gamma energy spectra and the primary PG energy spectra after 150 MeV proton irradiation between 1 and 8 MeV. Figure S2 can be referred to as a reference for the gamma rays emitted in the 0–1 MeV range. Most of the peaks originate from spallation reactions, neutron capture or inelastic proton interactions. It should be noted that, as the tumor volume is a mixture of water +1% weight of metallic nanoparticles, all characteristic peaks for water were also present with the same intensities. Common PG peaks for water and peaks of interest for silicon are presented in Table 4. Most reactions are listed in [34,36].

For proton-induced reactions, a comparison between Figure 4a,b and c,d highlights that the most prominent PG emission peaks originates from secondary processes such  $(n,\gamma)$  nuclear reactions. The interactions of the proton beam within the patient inevitably lead to neutron production, that in turn generate secondary nuclear reactions, resulting in an unintended dose. For instance, the 2.23 MeV peak results from neutron capture by hydrogen nuclei, namely  ${}^1\text{H}(n,\gamma){}^2\text{H}$ .  ${}^{113}\text{Cd}$  has a very high cross section for thermal neutron capture ( $\sim 20,600$  b), giving rise to numerous peaks below 1 MeV (cfr. Figure S2) and two intense higher energy peaks at 4.44 and 4.79 MeV [37].  ${}^{157}\text{Gd}$  also produced an intense peak at 7.937 MeV [33]. Other prominent rays can be identified at 6.512, 6.81, 7.28, and 7.63 MeV after the bombardment of  ${}^{197}\text{Au}$ ,  ${}^{107}\text{Ag}$ ,  ${}^{109}\text{Ag}$  and  ${}^{177}\text{Hf}$ , respectively. The relative importance of secondary processes when investigating the proton range through NP use can also be observed by analyzing Table 3. Ratios that are much smaller than the water equivalent value represent pollution in the PG signal and to additional doses in the patient, discarding Gd and Cd NP, and, to a lesser degree, Hf NP.

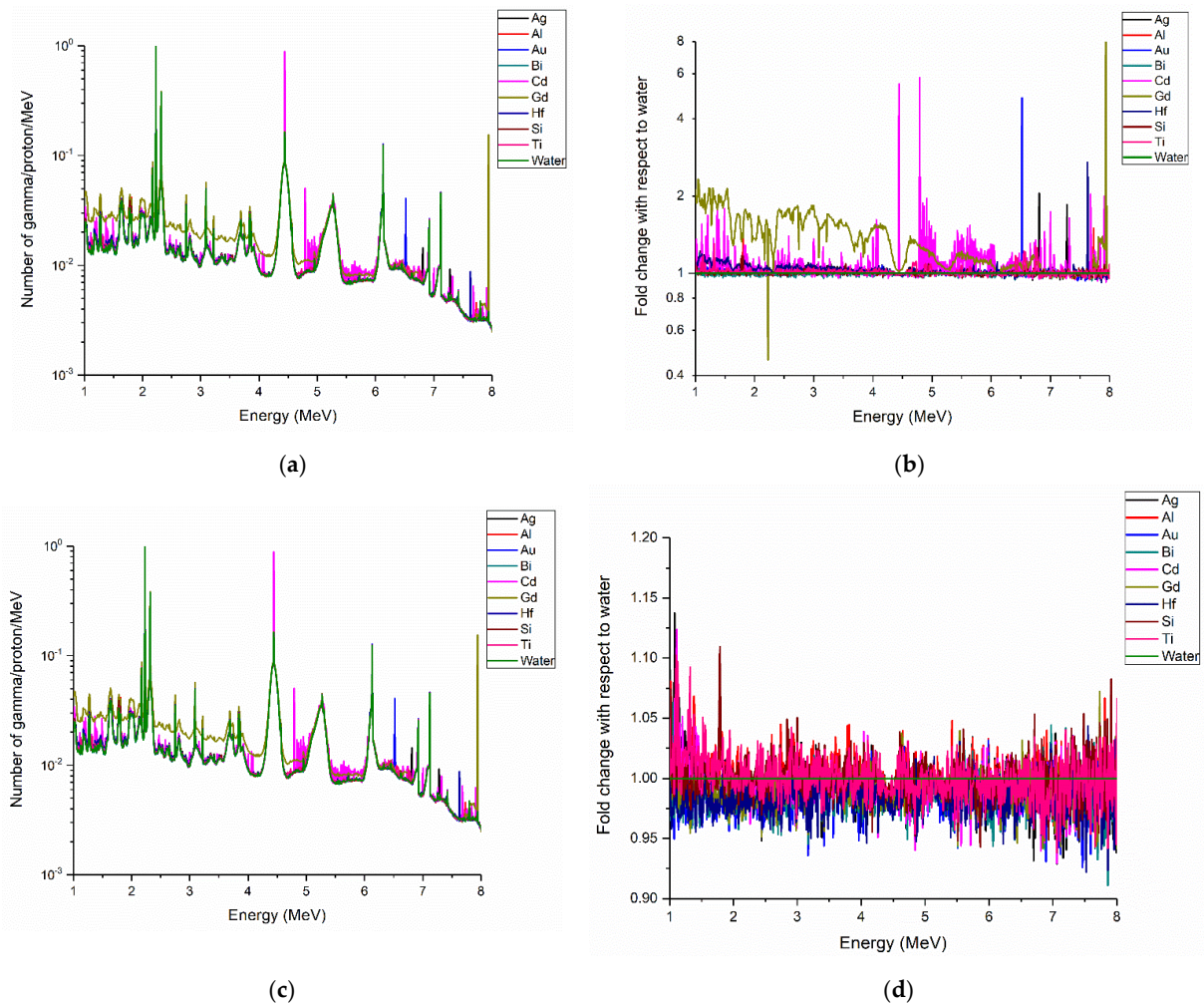


**Figure 4.** (a) Energy spectra of all gamma generated after 150 MeV proton irradiation and (b) corresponding fold change with respect to water. (c) Energy spectra of primary gamma generated after 150 MeV proton irradiation and (d) corresponding fold change with respect to water.

**Table 4.** Common prompt gamma rays from oxygen-16 and silicon-28, observed for the simulated tumor volume.

Peaks (MeV)	Prompt Gamma Reactions
Water	
1.022	$^{16}\text{O} (p,x) ^{10}\text{B}^*$
1.635	$^{16}\text{O} (p,x) ^{14}\text{N}^*$
2.313	$^{16}\text{O} (p,x) ^{14}\text{N}^*$
2.742	$^{16}\text{O} (p,p') ^{16}\text{O}^*$
3.684	$^{16}\text{O} (p,x) ^{13}\text{C}^*$
3.853	$^{16}\text{O} (p,x) ^{13}\text{C}^*$
4.438	$^{16}\text{O} (p,x) ^{12}\text{C}^*$
5.240	$^{16}\text{O} (p,x) ^{15}\text{O}^*$
5.269	$^{16}\text{O} (p,x) ^{15}\text{N}^*$
5.298	$^{16}\text{O} (p,x) ^{15}\text{N}^*$
6.129	$^{16}\text{O} (p,p') ^{16}\text{O}^*$
6.175	$^{16}\text{O} (p,x) ^{15}\text{O}^*$
6.916	$^{16}\text{O} (p,p') ^{16}\text{O}^*$
7.115	$^{16}\text{O} (p,p') ^{16}\text{O}^*$
Silicon	
1.014	$^{28}\text{Si} (p,x) ^{27}\text{Al}^*$
1.779	$^{28}\text{Si} (p,p') ^{28}\text{Si}^*$

p = incoming proton, p' = scattered proton, x = ejected fragment, \* = excited state of the nucleus.

A closer look at Figure 4c,d highlights an interesting emission peak found for SiNP at 1.779 MeV. Figure 5 presents the fold change with respect to water of primary PG from the tumor volume loaded with 1%wt SiNP or 1% wt AlNP. The 1.779 MeV PG emission peak on Figure 5a originates from the proton interaction through the  $^{28}\text{Si}(p,n)^{28}\text{P}^*$  process. However, another competing reaction,  $^{28}\text{Si}(n,p)^{28}\text{Al}^*$ , produces radioactive aluminum nuclides that relax at an identical energy. For cross sections of approximately the same order of magnitude, it may be difficult to precisely estimate the contribution of the  $(p,n\gamma)$  reaction that relates to the proton beam position [34,38,39]. A low energy PG emission peak at 1.014 MeV was observed for both SiNP and AlNP with similar intensities, resulting from  $^{28}\text{Si}(p,x)^{27}\text{Al}^*$  and  $^{27}\text{Al}(p,p')^{27}\text{Al}^*$  reactions (Figure 5a,b). In the case of AlNP, the  $^{27}\text{Al}(p,x)^{26}\text{Mg}^*$  reaction gave rise to the 1.809 MeV peak, contributing to the PG signal, although to a lesser extent. No identifiable peak was observed in the case of BiNPs.

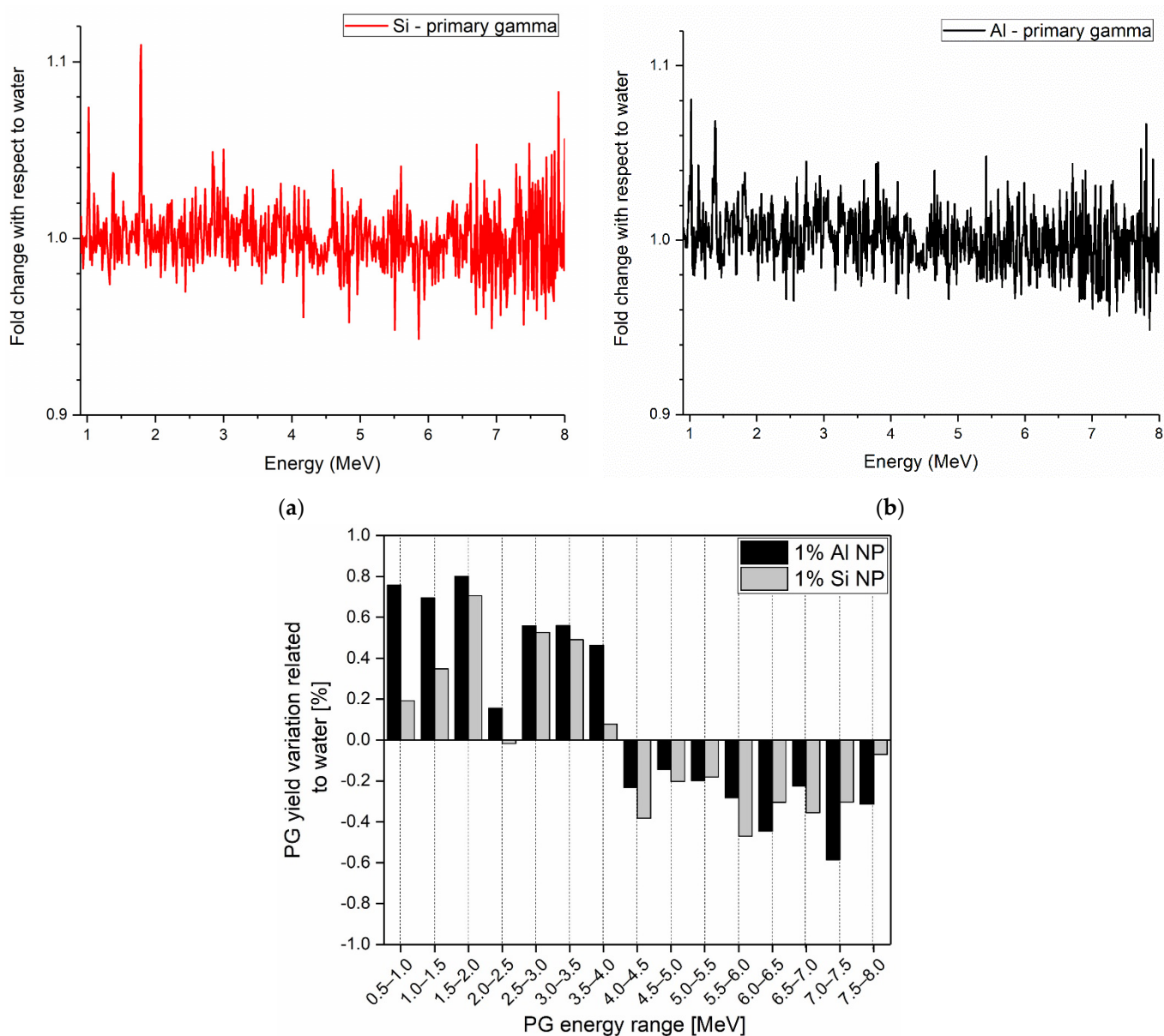


**Figure 5.** Energy spectra of primary gamma generated after 150 MeV proton irradiation on target (a) Si or (b) Al 1%wt. (c) Corresponding energy histogram (bin size = 500 keV). Results are expressed compared to prompt gamma yield in water.

#### 4. Discussion

To verify the range of a proton beam inside the patient, different properties of prompt gamma radiation can be used, leading to several clinical scenarios. In the more common scenario, known as PG imaging (PGI), the correlation of nuclear reaction positions with the energy deposition is used to image the spatial distribution of the deposited dose in the patient. PG timing (PGT), on the other hand, is based on the relationship between proton range and the travel time of particles before stopping [40]. Finally, the capacity to detect the emission of discrete energy  $\gamma$ -rays originating from the de-excitation of specific nuclei leads to PG spectroscopy (PGS) [36].

The aim of this study was to evaluate the potential benefits of metal-based nanoparticles in range-verification applications. The results obtained in this study reveals that the presence of NP with a mass fraction of 1% wt leads to a higher primary gamma yield at 80% PG fall off. Among the tested materials, only AlNP, BiNP and SiNP produced a ratio between the primary and secondary PG yield of higher than the one observed for water, despite the fact that they displayed only a moderate increase of only 3%, 3% and 6% at 80% PG fall off, respectively.

Although the reported increase in  $\gamma$ -ray emission might improve PGI, it must be observed in an energy range between 3 and 6 MeV, corresponding to the signal-to-noise ratio that provides the highest correlation to the end of proton track [41]. The simulations did not suggest a higher PG yield for any of the three metals compared to water in the useful energy range (cfr. Figure 5c), limiting the advantages of nanoparticles in PGI. However, a modest increase in  $\gamma$ -rays production is expected below 3 MeV for SiNP and AlNP. No increase was reported for BiNP. Since the addition of a temporal discrimination in the signal allows for a reduction in energy threshold to a range between 1 and 2 MeV, a potential benefit of NP for range verification, especially AlNP, might be observed in PGT clinical scenarios [41]. For SiNP, the higher production of low-energy  $\gamma$ -rays is mainly due to the  $^{28}\text{Si}(p,p')^{28}\text{Si}^*$  and  $^{28}\text{Si}(p,x)^{27}\text{Al}^*$  nuclear reactions that emit 1.779 and 1.014 MeV  $\gamma$ -rays, respectively. Since the cross section of these reactions varies with the energy proton beam, the focus on these specific peaks makes the use of SiNP for PGS viable [34]. However, the resulting signal will be difficult to distinguish from (n, $\gamma$ ) processes and secondaries that take place at close energies.

In the scope of this work, we based our calculations on a 1% NP weight content in the tumor, a relevant concentration in light of in vivo NP mass fraction, which was reached after intravenous injection in mammals [30,31]. Moreover, this is several orders of magnitude higher than the maximal  $10^{-4}\%$  wt of silicon and aluminum content that is naturally present in tissues [42]. However, it is important to note that a major limitation of this study is that we considered a uniform distribution of 1% by mass throughout the tumor volume, rather than in discrete nanoscale volumes, impacting the probability of an energetic particle interacting with a metal element.

Although we were able to identify specific  $\gamma$ -rays on which the signal enhancement can be based, the reported fold change in PG yield remains too small to present it as a viable method for NP in range verification. However, the PG yield is directly proportional to NP concentration. Therefore, strategies to increase the metal loading in tumor such as the use of tumor targeted antibody-conjugated NP [43,44] or intra-tumoral injection [45] constitute a working hypothesis to enhance PG signal. This assumes that (i) the NP distribution is homogeneous in the tumor and that (ii) the NP loading in tumor, compared to the loading in surrounding tissues, is very high. These features are critical to ensure an accurate beam range verification, since we reported that NP induces a Bragg-peak shift that increases with the metal concentration in the tumor and the atomic number of NP. For SiNP, this shift represents 1% and 3% of the beam range for 1% and 10% wt Si loading in the tumor, respectively (cfr. Figure S3). Note that the magnitude of this shift increases with the atomic number of nanomaterials. Therefore, if the uncertainty over NP distributions in the PTV is unknown, it contributes to range uncertainties, resulting in a PG detection profile that is challenging to interpret. This highlights the importance of accurately characterizing

NP distribution so as to adapt treatment plans and ensure the correct irradiation of tumor distal edge. Moreover, it highlights the need for range verification when proton therapy treatments are used in combination with radiosensitizers made of elements with a high atomic number.

## 5. Conclusions

The use of metal-based nano-objects to improve proton range verification has faced challenges inherent to the targeted application of the systemic injection of any molecule in clinical applications [24,46]. First, the PG camera design favors the counting rate over energy resolution. In this configuration, our results showed the ratio between the total number of primary PG and secondary PG to be only slightly improved below 3 MeV compared to water (1% wt NP in tumor). Second, the development of new nano-objects for better targeting, and a homogeneous NP distribution in the PTV, has to be undertaken to accurately identify the Bragg peak position. Since in vivo experiments evidenced non-homogeneous NP distribution in tumor, and the uncertainty is not quantifiable at this stage, additional range uncertainties are associated with the use of NP.

The simulations performed in this study show a weak proof-of-concept that does not seem to be translatable for a clinical application in realistic scenarios. In this case, we can expect a lower metal mass reached in the PTV coupled with a non-homogeneous distribution, which will further limit the PG yield. The benefit of using metallic nanoparticles in protontherapy treatments seems to mainly reside in their radioenhancement effect, in secondary Auger and protoelectrons emission (the so-called physical effect) [47], their radiosensitization effect, cells detoxification system impairment (biological effect induced prior to radiation exposure) [48,49], and in the production of short-lived beta emitters, such as  $^{28}\text{Al}$  in the case of SiNPs. Originating from the neutron capture of metal isotopes, these beta emitters may locally enhance the deposited dose in the tumor, with the help of NP active targeting. Further investigations are still needed to estimate the additional contribution to the deposited dose in this approach.

The use of NP for range verification seems to be very limited due to the aforementioned hurdles. However, medical devices filled with a high content of Al or Si can be used to detect overshoot during treatments, without the requirement of a systemic injection of the nano-objects. Endorectal balloons, used to stabilize prostate movement during its treatment, filled with these elements may help to monitor rectal radiation exposure based on an increased PG yield [50].

**Supplementary Materials:** The following are available online at <https://www.mdpi.com/article/10.3390/radiation1040025/s1>, Figure S1: Normalized dose distribution after 150 MeV proton irradiation (left axis) and longitudinal distribution of all gamma rays emitted with energies higher than 1 MeV (right axis) (zoom on the “Tumor area”), Figure S2: Energy spectra ratio to water of gamma rays generated after 150 MeV proton irradiation, limited to the 0-1 MeV range for (a) all gammas or (b) only primary PG, Figure S3: Bragg peak shift according to NP weight percent in tumor and NP atomic number.

**Author Contributions:** Methodology: A.-C.H., S.L. & F.H.; Investigation: S.P. & F.H.; Writing: S.P. & F.H.; Review and editing: J.S., J.L.C., S.L. & A.-C.H.; Supervision: A.-C.H. All authors have read and agreed to the published version of the manuscript.

**Funding:** This research was funded by European Union’s H2020 Research and Innovation Programme, under Grant Agreement No: 730983 and the Walloon Region through Protherwal project (grant agreement No: 7289).

**Conflicts of Interest:** The authors declare no conflict of interest.

## References

1. Paganetti, H. *Proton Therapy Physics*; CRC Press: Boca Raton, FL, USA, 2018.
2. Paganetti, H.; Beltran, C.; Both, S.; Dong, L.; Flanz, J.; Furutani, K.; Grassberger, C.; Grosshans, D.R.; Knopf, A.-C.; Langendijk, J.A. Roadmap: Proton therapy physics and biology. *Phys. Med. Biol.* **2021**, *66*, 05RM01. [[CrossRef](#)] [[PubMed](#)]

3. Yang, M.; Virshup, G.; Clayton, J.; Zhu, X.R.; Mohan, R.; Dong, L. Theoretical variance analysis of single-and dual-energy computed tomography methods for calculating proton stopping power ratios of biological tissues. *Phys. Med. Biol.* **2010**, *55*, 1343. [[CrossRef](#)]
4. Bourque, A.E.; Carrier, J.-F.; Bouchard, H. A stoichiometric calibration method for dual energy computed tomography. *Phys. Med. Biol.* **2014**, *59*, 2059. [[CrossRef](#)] [[PubMed](#)]
5. Paganetti, H. Range uncertainties in proton therapy and the role of Monte Carlo simulations. *Phys. Med. Biol.* **2012**, *57*, R99. [[CrossRef](#)]
6. Knopf, A.-C.; Lomax, A. In vivo proton range verification: A review. *Phys. Med. Biol.* **2013**, *58*, R131. [[CrossRef](#)]
7. Gioscio, E.; Battistoni, G.; Bochetti, A.; de Simoni, M.; Dong, Y.; Fischetti, M.; Mattei, I.; Mirabelli, R.; Muraro, S.; Patera, V. Development of a novel neutron tracker for the characterisation of secondary neutrons emitted in Particle Therapy. *Nucl. Instrum. Methods Phys. Res. Sect. A Accel. Spectrometers Detect. Assoc. Equip.* **2020**, *958*, 162862. [[CrossRef](#)]
8. Marafini, M.; Gasparini, L.; Mirabelli, R.; Pinci, D.; Patera, V.; Sciubba, A.; Spiriti, E.; Stoppa, D.; Traini, G.; Sarti, A. MONDO: A neutron tracker for particle therapy secondary emission characterization. *Phys. Med. Biol.* **2017**, *62*, 3299. [[CrossRef](#)] [[PubMed](#)]
9. Assmann, W.; Kellnberger, S.; Reinhardt, S.; Lehrack, S.; Edlich, A.; Thirolf, P.; Moser, M.; Dollinger, G.; Omar, M.; Ntziachristos, V. Ionoacoustic characterization of the proton Bragg peak with submillimeter accuracy. *Med. Phys.* **2015**, *42*, 567–574. [[CrossRef](#)]
10. Jones, K.C. *Acoustic-Based Proton Range Verification, Radiation Therapy Dosimetry: A Practical Handbook*; CRC Press: Boca Raton, FL, USA, 2021; pp. 443–456.
11. Ferrero, V.; Fiorina, E.; Morrocchi, M.; Pennazio, F.; Baroni, G.; Battistoni, G.; Belcari, N.; Ciocca, M.; del Guerra, A.; Donetti, M. Online proton therapy monitoring: Clinical test of a Silicon-photodetector-based in-beam PET. *Sci. Rep.* **2018**, *8*, 4100. [[CrossRef](#)]
12. Pennazio, F.; Battistoni, G.; Bisogni, M.G.; Camarlinghi, N.; Ferrari, A.; Ferrero, V.; Fiorina, E.; Morrocchi, M.; Sala, P.; Sportelli, G. Carbon ions beam therapy monitoring with the INSIDE in-beam PET. *Phys. Med. Biol.* **2018**, *63*, 145018. [[CrossRef](#)]
13. Yamaguchi, M.; Nagao, Y.; Ando, K.; Yamamoto, S.; Toshito, T.; Kataoka, J.; Kawachi, N. Secondary-electron-bremsstrahlung imaging for proton therapy. *Nucl. Instrum. Methods Phys. Res. Sect. A Accel. Spectrometers Detect. Assoc. Equip.* **2016**, *833*, 199–207. [[CrossRef](#)]
14. Min, C.-H.; Kim, C.H.; Youn, M.-Y.; Kim, J.-W. Prompt gamma measurements for locating the dose falloff region in the proton therapy. *Appl. Phys. Lett.* **2006**, *89*, 183517. [[CrossRef](#)]
15. Martins, P.M.; Bello, R.D.; Seco, J. *Prompt Gamma Detection for Proton Range Verification, Radiation Therapy Dosimetry: A Practical Handbook*; CRC Press: Boca Raton, FL, USA, 2021; pp. 427–442.
16. Jongens, Y.; Stichelbaut, F. Verification of the proton beams position in the patient by the detection of prompt gamma-rays emission. In Proceedings of the 39th Meeting of the Particle Therapy Co-Operative Group, San Francisco, CA, USA, 26–29 October 2003.
17. Richter, C.; Pausch, G.; Barczyk, S.; Priegnitz, M.; Keitz, I.; Thiele, J.; Smeets, J.; Stappen, F.V.; Bombelli, L.; Fiorini, C. First clinical application of a prompt gamma based in vivo proton range verification system. *Radiother. Oncol.* **2016**, *118*, 232–237. [[CrossRef](#)] [[PubMed](#)]
18. Xie, Y.; Bentefour, E.H.; Janssens, G.; Smeets, J.; Stappen, F.V.; Hotoiu, L.; Yin, L.; Dolney, D.; Avery, S.; O’Grady, F. Prompt gamma imaging for in vivo range verification of pencil beam scanning proton therapy. *Int. J. Radiat. Oncol. Biol. Phys.* **2017**, *99*, 210–218. [[CrossRef](#)]
19. Pinto, M.; Dauvergne, D.; Freud, N.; Krimmer, J.; Létang, J.M.; Testa, E. Assessment of Geant4 prompt-gamma emission yields in the context of proton therapy monitoring. *Front. Oncol.* **2016**, *6*, 10. [[CrossRef](#)] [[PubMed](#)]
20. Zarifi, M.; Guatelli, S.; Qi, Y.; Bolst, D.; Prokopovich, D.; Rosenfeld, A. Characterization of prompt gamma ray emission for in vivo range verification in particle therapy: A simulation study. *Phys. Med.* **2019**, *62*, 20–32. [[CrossRef](#)]
21. Zarifi, M.; Guatelli, S.; Bolst, D.; Hutton, B.; Rosenfeld, A.; Qi, Y. Characterization of prompt gamma-ray emission with respect to the Bragg peak for proton beam range verification: A Monte Carlo study. *Phys. Med.* **2017**, *33*, 197–206. [[CrossRef](#)]
22. Agostinelli, S.; Allison, J.; Amako, K.a.; Apostolakis, J.; Araujo, H.; Arce, P.; Asai, M.; Axen, D.; Banerjee, S.; Barrand, G. GEANT4—A simulation toolkit. *Nucl. Instrum. Methods Phys. Res. Sect. A: Accel. Spectrometers Detect. Assoc. Equip.* **2003**, *506*, 250–303. [[CrossRef](#)]
23. Allison, J.; Amako, K.; Apostolakis, J.; Arce, P.; Asai, M.; Aso, T.; Bagli, E.; Bagulya, A.; Banerjee, S.; Barrand, G. Recent developments in Geant4. *Nucl. Instrum. Methods Phys. Res. Sect. A Accel. Spectrometers Detect. Assoc. Equip.* **2016**, *835*, 186–225. [[CrossRef](#)]
24. Penninckx, S.; Heuskin, A.-C.; Michiels, C.; Lucas, S. Gold nanoparticles as a potent radiosensitizer: A transdisciplinary approach from physics to patient. *Cancers* **2020**, *12*, 2021. [[CrossRef](#)]
25. Schuemann, J.; Bagley, A.F.; Berbeco, R.; Bromma, K.; Butterworth, K.T.; Byrne, H.L.; Chithrani, B.D.; Cho, S.H.; Cook, J.R.; Favaudon, V. Roadmap for metal nanoparticles in radiation therapy: Current status, translational challenges, and future directions. *Phys. Med. Biol.* **2020**, *65*, 21RM02. [[CrossRef](#)]
26. Li, S.; Penninckx, S.; Karmani, L.; Heuskin, A.C.; Watillon, K.; Marega, R.; Zola, J.; Corvaglia, V.; Genard, G.; Gallez, B.; et al. LET-dependent radiosensitization effects of gold nanoparticles for proton irradiation. *Nanotechnology* **2016**, *27*, 455101. [[CrossRef](#)] [[PubMed](#)]

27. Bolst, D.; Cirrone, G.A.; Cuttone, G.; Folger, G.; Incerti, S.; Ivanchenko, V.; Koi, T.; Mancusi, D.; Pandola, L.; Romano, F. Validation of Geant4 fragmentation for heavy ion therapy. *Nucl. Instrum. Methods Phys. Res. Sect. A: Accel. Spectrometers Detect. Assoc. Equip.* **2017**, *869*, 68–75. [[CrossRef](#)]
28. Jarlskog, C.Z.; Paganetti, H. Physics Settings for Using the Geant4 Toolkit in Proton Therapy. *IEEE Trans. Nucl. Sci.* **2008**, *55*, 1018–1025. [[CrossRef](#)]
29. ICRU. *37 Stopping Powers for Electrons and Positrons*; International Commission on Radiation Units and Measurements: Bethesda, MD, USA, 1984.
30. Hainfeld, J.; Smilowitz, H.; O'Connor, M.; Dilmanian, F.; Slatkin, D. Gold nanoparticle imaging and radiotherapy of brain tumors in mice. *Nanomedicine* **2013**, *8*, 1601–1609. [[CrossRef](#)]
31. Hainfeld, J.F.; Slatkin, D.N.; Smilowitz, H.M. The use of gold nanoparticles to enhance radiotherapy in mice. *Phys. Med. Biol.* **2004**, *49*, N309. [[CrossRef](#)]
32. Sung, W.; Schuemann, J. Energy optimization in gold nanoparticle enhanced radiation therapy. *Phys. Med. Biol.* **2018**, *63*, 135001. [[CrossRef](#)]
33. Tanaka, T.; Hagiwara, K.; Gazzola, E.; Ali, A.; Ou, I.; Sudo, T.; Das, P.K.; Reen, M.S.; Dhir, R.; Koshio, Y. Gamma-ray spectra from thermal neutron capture on gadolinium-155 and natural gadolinium. *Prog. Theor. Exp. Phys.* **2020**, *2020*, 043D002. [[CrossRef](#)]
34. Kozlovsky, B.; Murphy, R.J.; Ramaty, R. Nuclear deexcitation gamma-ray lines from accelerated particle interactions. *Astrophys. J. Suppl. Ser.* **2002**, *141*, 523. [[CrossRef](#)]
35. Demortier, G.; Bodart, F. Quantitative analysis of phosphorus by (p,g) reactions—LARN report 711. In Proceedings of the International Meeting on Chemical Analysis by charged Particles Bombardment, Namur, Belgium, 6–8 September 1971.
36. Verburg, J.M.; Seco, J. Proton range verification through prompt gamma-ray spectroscopy. *Phys. Med. Biol.* **2014**, *59*, 7089–7106. [[CrossRef](#)]
37. Pringle, R.; Taylor, H.; Roulston, K. Radiative Capture of Thermal Neutrons by Cd 113. *Phys. Rev.* **1952**, *87*, 1016. [[CrossRef](#)]
38. Sadler, G.; Jarvis, O.; van Belle, P.; Pillon, M. Use of the  $^{28}\text{Si}(n,p)^{28}\text{Al}$  reaction for the measurement of 14 MeV neutrons from fusion plasmas. *Rev. Sci. Instrum.* **1990**, *61*, 3175–3177. [[CrossRef](#)]
39. Mannhart, W.; Schmidt, D. Measurement of the  $^{28}\text{Si}(n,p)$ ,  $^{29}\text{Si}(n,p)$  and  $^{30}\text{Si}(n,\alpha)$  Cross Sections between 6.9 and 14.0 MeV. *J. Nucl. Sci. Technol.* **2002**, *39*, 218–221. [[CrossRef](#)]
40. Golnik, C.; Hueso-González, F.; Müller, A.; Dendooven, P.; Enghardt, W.; Fiedler, F.; Kormoll, T.; Roemer, K.; Petzoldt, J.; Wagner, A. Range assessment in particle therapy based on prompt  $\gamma$ -ray timing measurements. *Phys. Med. Biol.* **2014**, *59*, 5399. [[CrossRef](#)] [[PubMed](#)]
41. Lopes, P.C.; Clementel, E.; Crespo, P.; Henrotin, S.; Huizenga, J.; Janssens, G.; Parodi, K.; Prieels, D.; Roellinghoff, F.; Smeets, J. Time-resolved imaging of prompt-gamma rays for proton range verification using a knife-edge slit camera based on digital photon counters. *Phys. Med. Biol.* **2015**, *60*, 6063. [[CrossRef](#)]
42. Austin, J. Silicon Levels in Human Tissues. In *Biochemistry of Silicon and Related Problems*; Bendz, G., Lindqvist, I., Runnström-Reio, V., Eds.; Springer: Boston, MA, USA, 1978.
43. Karmani, L.; Labar, D.; Valembois, V.; Bouchat, V.; Nagaswaran, P.G.; Bol, A.; Gillart, J.; Levêque, P.; Bouzin, C.; Bonifazi, D. Antibody-functionalized nanoparticles for imaging cancer: Influence of conjugation to gold nanoparticles on the biodistribution of  $^{89}\text{Zr}$ -labeled cetuximab in mice. *Contrast Media Mol. Imaging* **2013**, *8*, 402–408. [[CrossRef](#)]
44. Li, S.; Bouchy, S.; Penninckx, S.; Marega, R.; Fichera, O.; Gallez, B.; Feron, O.; Martinive, P.; Heuskin, A.C.; Michiels, C.; et al. Antibody-functionalized gold nanoparticles as tumor targeting radiosensitizers for proton therapy. *Nanomedicine* **2019**, *14*, 317–333. [[CrossRef](#)]
45. Durymanov, M.O.; Rosenkranz, A.A.; Sobolev, A.S. Current Approaches for Improving Intratumoral Accumulation and Distribution of Nanomedicines. *Theranostics* **2015**, *5*, 1007–1020. [[CrossRef](#)]
46. Tremi, I.; Spyratou, E.; Souli, M.; Efstathopoulos, E.P.; Makropoulou, M.; Georgakilas, A.G.; Sihver, L. Requirements for Designing an Effective Metallic Nanoparticle (NP)-Boosted Radiation Therapy (RT). *Cancers* **2021**, *13*, 3185. [[CrossRef](#)]
47. Heuskin, A.C.; Gallez, B.; Feron, O.; Martinive, P.; Michiels, C.; Lucas, S. Metallic nanoparticles irradiated by low-energy protons for radiation therapy: Are there significant physical effects to enhance the dose delivery? *Med. Phys.* **2017**, *44*, 4299–4312. [[CrossRef](#)]
48. Penninckx, S.; Heuskin, A.C.; Michiels, C.; Lucas, S. The role of thioredoxin reductase in gold nanoparticle radiosensitization effects. *Nanomedicine* **2018**, *13*, 2917–2937. [[CrossRef](#)] [[PubMed](#)]
49. Penninckx, S.; Heuskin, A.C.; Michiels, C.; Lucas, S. Thioredoxin Reductase Activity Predicts Gold Nanoparticle Radiosensitization Effect. *Nanomaterials* **2019**, *9*, 295. [[CrossRef](#)] [[PubMed](#)]
50. Martins, P.M.; Freitas, H.; Tessonnier, T.; Ackermann, B.; Brons, S.; Seco, J. Towards real-time PGS range monitoring in proton therapy of prostate cancer. *Sci. Rep.* **2021**, *11*, 15331. [[CrossRef](#)] [[PubMed](#)]